

Simulations of slip flow on nanobubble-laden surfaces

J. Hyväluoma¹, C. Kunert², and J. Harting^{3,2}

¹ MTT Agrifood Research Finland, FI-31600 Jokioinen, Finland

² Institute for Computational Physics, University of Stuttgart, Pfaffenwaldring 27, D-70569 Stuttgart, Germany

³ Department of Applied Physics, Eindhoven University of Technology, Den Dolech 2, NL-5600MB Eindhoven, The Netherlands

E-mail: j.harting@tue.nl

Abstract. On microstructured hydrophobic surfaces, geometrical patterns may lead to the appearance of a superhydrophobic state, where gas bubbles at the surface can have a strong impact on the fluid flow along such surfaces. In particular, they can strongly influence a detected slip at the surface. We present two-phase lattice Boltzmann simulations of a flow over structured surfaces with attached gas bubbles and demonstrate how the detected slip depends on the pattern geometry, the bulk pressure, or the shear rate. Since a large slip leads to reduced friction, our results allow to assist in the optimization of microchannel flows for large throughput.

PACS numbers: 83.50.Rp, 47.11.j, 47.55.D

Submitted to: *J. Phys.: Condens. Matter*

1. Introduction

The impressive success of the miniaturization of technical devices down to submicrometric sizes has led to numerous practically applicable devices which are used for the manipulation and transport fluids. Such microfluidic devices include micromixers, DNA amplifiers, chromatography systems, or chemical reactors. However, in order to fully understand the properties of such devices and to optimise them for efficient usage, some fundamental questions in physics including the behavior of single molecules in fluid flow or the validity of the no-slip boundary condition have to be answered [1, 2]. While for gas flows at large Knudsen number rarefaction effects that can result in a slippage of the flow at surfaces are expected, for liquids one would naively assume that its velocity close to a surface always corresponds to the actual velocity of the surface itself. This assumption is called the no-slip boundary condition and can be accounted for as one of the generally accepted fundamental concepts of fluid mechanics. However, this concept was not always well accepted. Some centuries ago there were long debates about the velocity of a Newtonian liquid close to a surface and the acceptance of the no-slip boundary condition was mostly due to the fact that no experimental violations could be found, i.e., a so-called boundary slip could not be detected.

Recently, well controlled experiments have shown a violation of the no-slip boundary condition in sub-micron sized geometries. Since then, mostly experimental [2–9, 4] but also theoretical works [10, 11], as well as computer simulations [12–16] have been performed to improve our understanding of slippage. An (apparent) violation of the no-slip boundary condition can be explained by the complex behavior of a fluid close to a solid interface which involves the interplay of many physical and chemical properties. These include the wettability of the solid, the shear rate or flow velocity, the bulk pressure, the surface charge, the surface roughness, as well as impurities, dissolved gas, or bubbles attached to surfaces. Due to the large number of different parameters, a significant dispersion of the results can be observed for almost similar systems [2, 17]. For example, observed slip lengths vary between a few nanometres [18] and micrometres [4] and while some authors find a dependence of the slip on the flow velocity [6, 19, 3], others do not [5, 4]. Extensive reviews of the slip phenomenon have recently been published by Lauga et al. [2], Neto et al. [17], as well as Bocquet and Barrat [20].

A boundary slip is typically quantified by the so-called slip length b – a concept that was already proposed by Navier in 1823. He introduced a boundary condition where the fluid velocity at a surface is proportional to the shear rate at the surface [21] (at $x = x_0$), i.e.,

$$u_z(x_0) = b \frac{\partial u_z(x)}{\partial x}. \quad (1)$$

In other words, the slip length b can be defined as the distance from the surface where the flow velocity vanishes.

During the last few years, the substantial scientific research invested in the slip

phenomenon has led to a more clear picture which can be summarized as follows: one can argue that many surprising results published were only due to artefacts or misinterpretation of experiments. In general, there seems to be an agreement within the community that the no-slip boundary condition is a valid assumption for smooth hydrophilic surfaces down to contact [9, 22, 23]. Slip lengths larger than a few nanometres can usually be referred to as “apparent slip” and are often caused by experimental artefacts or not fully understood effects. Examples for those can be surface structures, variations in the local contact angle at the surface or dissolved gases forming nano- or microscale bubbles on the surface. It is also possible to utilize such surface properties in order to generate bubbles in a controlled way so as to add slippery surfaces to the flow channel and thereby increase the slip length and reduce the viscous friction. An example that has lately gathered a lot of interest are surfaces that are patterned with arrays of holes where gas bubbles are attached to the holes [24–29]. Although reasonably flat bubbles lead to increased effective slip lengths, it has recently been observed that bubbles strongly protruding to the flow channel may actually have an opposite effect, i.e., they may reduce the slip and increase the hydrodynamic drag [24]. Numerical studies have predicted even a possibility of negative slip lengths [24, 25, 28]. The enhanced friction can be understood with help of the additional roughness produced by the bubbles which can overcome the lubricating effect of the stress-free liquid-gas interfaces. The numerical results of negative slip lengths were recently verified in theoretical investigation of Davis and Lauga [26].

In all studies concerning slip flow over a bubble mattress we are aware of, the mattress under consideration has been built up of evenly sized and equally shaped bubbles. However, as real configurations inevitably include some kind of imperfections, it would also be interesting to know whether the disorder in the mattress affects the detected slip behavior. Therefore, in this paper a case where the mattress is made up of bubbles of two different sizes is considered. In practice, such a situation is achieved by structuring the surface with holes that have different radii. This structuring leads, for a given bulk pressure, to a bubble configuration where bubbles located in larger holes protrude stronger to the flow channel than those in the smaller ones. In particular, we show that the bubble-size distribution can significantly affect the slip behavior and, e.g., decrease the negative slip caused by strongly protruding bubbles. While this reduction may hamper experimental observations of negative slip, it may on the other hand be utilized in designing bubble surfaces aiming to maximal flow slippage.

2. Lattice Boltzmann simulations to investigate boundary slip

The simulation method used to study microfluidic devices has to be chosen carefully. Molecular dynamics simulations (MD) are the best choice to simulate the fluid-wall interaction, but the presently available computer power is not sufficient to simulate length and time scales necessary to achieve orders of magnitude which are relevant for experiments. However, boundary slip with a slip length b of the order of many

molecular diameters has been studied with molecular dynamics simulations by various authors [7, 14, 15, 30, 31].

The current contribution focuses on numerical investigations of the slip phenomenon by means of lattice Boltzmann simulations. It should be noticed that while a large number of groups utilizes the lattice Boltzmann technique to investigate microfluidic problems, only a very small number of researchers is actually applying the method to study slippage. This is surprising since mesoscopic simulation methods offer a closer relation to experimentally relevant time and length scales than microscopic techniques such as molecular dynamics, even though the interactions between fluids and surfaces have to be described on a mesoscopic scale in the lattice Boltzmann method.

Within the lattice Boltzmann method a popular approach is to introduce slip by generalizing the no-slip bounce-back boundary conditions in order to allow specular reflections with a given probability [12, 16, 32, 33], or to apply diffuse scattering [34–36]. It has been shown by Guo et al. that these approaches are virtually equivalent [37]. Another possibility is to modify the fluid viscosity due to local density variations in order to model slip [38]. In both cases, the parameters determining the properties at the boundaries are “artificial” parameters and they do not have any obvious physical meaning. Therefore, these parameters are not easily mappable to experimentally available quantities. We model the interaction between hydrophobic channel walls and the fluid by means of a multiphase lattice Boltzmann model. Our approach overcomes this problem by applying a mesoscopic force between the walls and the fluid. A similar approach is used by Zhu et al. [39], Benzi et al. [40], and Zhang et al. [41]. This force applied at the boundary can be linked to the contact angle which is commonly used by experimentalists to quantitatively describe the wettability of materials [42–45]. While we are not aware of further lattice Boltzmann simulations to study the flow over a bubble mattress, a number of authors has applied various lattice Boltzmann multiphase and multicomponent models to study the properties of droplets on chemically patterned and superhydrophobic surfaces [46–50].

The lattice Boltzmann method is based on the Boltzmann kinetic equation

$$\left[\frac{\partial}{\partial t} + \mathbf{u} \cdot \nabla_{\mathbf{x}} \right] f(\mathbf{x}, \mathbf{u}, t) = \Omega, \quad (2)$$

which is discretized on a lattice. The Boltzmann equation describes the evolution of the single particle probability density $f(\mathbf{x}, \mathbf{u}, t)$, where \mathbf{x} is the position, \mathbf{u} the velocity, and t the time. The derivatives on the left-hand side represent propagation of particles in phase space whereas the collision operator Ω takes into account molecular collisions. When discretized, to represent the correct hydrodynamics, the collision operator should conserve mass and momentum, and it should ensure sufficient isotropy and be Galilean invariant. By performing a Chapman-Enskog analysis, it can be shown that such a collision operator Ω leads to flow behavior following the Navier-Stokes equation [51]. In the lattice Boltzmann method the time t , the position \mathbf{x} , and the velocity \mathbf{u} are discretized leading to a discretized version of Eq. 2:

$$f_i(\mathbf{x} + \mathbf{c}_i, t + 1) - f_i(\mathbf{x}, t) = \Omega_i, \quad i = 0, 1, \dots, B. \quad (3)$$

Above, $f_i(\mathbf{x}, t)$ indicates the amount of fluid at site \mathbf{x} at time step t with velocity \mathbf{c}_i . Our simulations are performed on a three dimensional lattice with $B = 19$ discrete velocities (the so-called D3Q19 model). For the collision operator Ω_i we choose the Bhatnagar-Gross-Krook (BGK) form [52]

$$\Omega_i = -\frac{1}{\tau}(f_i(\mathbf{x}, t) - f_i^{eq}(\mathbf{u}(\mathbf{x}, t), \varrho(\mathbf{x}, t))) , \quad (4)$$

where τ is the mean collision time that determines the kinematic viscosity

$$\nu = \frac{2\tau - 1}{6}. \quad (5)$$

of the fluid. In this study the relaxation time τ is kept constant at value 1.0. Due to the collisions, the system relaxes towards an equilibrium distribution f_i^{eq} which can be derived imposing restrictions on the microscopic processes, such as explicit mass and momentum conservation. In our implementation we choose for the equilibrium distribution function

$$f_i^{eq} = \zeta_i \varrho \left[1 + \frac{\mathbf{c}_i \cdot \mathbf{u}}{c_s^2} + \frac{(\mathbf{c}_i \cdot \mathbf{u})^2}{2c_s^4} - \frac{u^2}{2c_s^2} \right], \quad (6)$$

which is a polynomial expansion of the Maxwell distribution where ζ_i are the lattice weights resulting from the velocity space discretization, and $c_s = 1/\sqrt{3}$ is the speed of sound for the D3Q19 lattice. The hydrodynamic quantities are obtained as moments of the single-particle distribution function $f_i(\mathbf{x}, t)$. For example, the density at lattice site \mathbf{x} is

$$\varrho(\mathbf{x}, t) \equiv \sum_i f_i(\mathbf{x}, t), \quad (7)$$

and the macroscopic velocity $\mathbf{u}(\mathbf{x}, t)$ is obtained from

$$\varrho(\mathbf{x}, t) \mathbf{u}(\mathbf{x}, t) \equiv \sum_i f_i(\mathbf{x}, t) \mathbf{c}_i. \quad (8)$$

Mean-field interactions between fluid particles are introduced by following the work of Shan and Chen, as a mean-field body force between nearest neighbours [53, 54],

$$\mathbf{F} = G_b \psi(\mathbf{r}) \sum_i \zeta_i \psi(\mathbf{r} + \mathbf{c}_i) \mathbf{c}_i, \quad (9)$$

where $\psi = 1 - \exp(-\varrho/\varrho_0)$ is an effective mass, G_b tunes the strength of the interaction, and ϱ_0 is a reference density. This force term leads to a non-ideal equation of state with pressure $P = c_s^2 \varrho + \frac{1}{2} c_s^2 G_b \psi^2$, and it enables simulations of liquid-vapor systems with surface tension. To model the wetting behavior at fluid-solid surfaces, a similar interaction is added between the fluid and solid phases, and the contact angle is tuned by setting a density value ϱ_w at the boundaries [55, 45]. Additionally, we apply mid-grid bounce back boundary conditions between the fluid and the surface which assures vanishing velocities at solid surfaces. Here, a distribution function that would be advected into a solid node is simply reversed and advected into the opposite direction [51].

From molecular dynamics simulations it is known that the fluid-wall interactions causing a slip phenomenon usually take place within a few molecular layers of the liquid

along the boundary surface [15, 14, 30, 7]. Our coarse-grained fluid wall interaction acts on the length scale of one lattice constant and does not take the molecular details into account. Therefore, coarse-grained implementations based on the lattice Boltzmann method are only able to reproduce an averaged effect of the interaction and cannot fully resolve the correct flow profile very close to the wall and below the resolution of a single lattice spacing. However, in order to understand the influence of the hydrophobicity on experimentally observed apparent slip, it is sufficient to investigate the flow behavior on more macroscopic scales as they are accessible for experimental investigation. Coarse-grained interaction models could be improved by a direct mapping of data obtained from MD simulations to the coupling constant G_b allowing a direct comparison of the influence of liquid-wall interactions on the detected slip [45]. Similar approaches are known from quantitative comparisons of lattice Boltzmann and molecular dynamics simulations in the literature [56, 57].

In recent years we studied the influence of a number of parameters on an apparent boundary slip using the method described above. Here, we shortly review the main conclusions of our previous findings. A more comprehensive review can be found in [58].

In [45], we showed that our mesoscopic approach is able to reach the small flow velocities of known experiments and reproduces results from experiments and other computer simulations, namely an increase of the slip with increasing liquid-solid interactions, the slip being independent of the flow velocity, and a decreasing slip with increasing bulk pressure [45].

If typical length scales of the system are comparable to the scale of surface roughness, the effect of roughness cannot be neglected anymore. The influence of surface variations on the slip length b has been investigated by numerous authors. It was demonstrated by Richardson that roughness leads to higher drag forces and thus to no-slip on macroscopic scales [59]. An experimental confirmation was later presented by McHale and Newton [60]. Sbragaglia et al. applied the LB method to simulate fluids in the vicinity of microstructured hydrophobic surfaces [55], Al-Zoubi et al. demonstrated that the LB method is well applicable to reproduce known flow patterns in sinusoidal channels [61], and Varnik et al. [62, 63] have shown that even in small geometries rough channel surfaces can cause flow to become turbulent. Recently, we presented the idea of an effective wall position at which the no-slip boundary condition holds for rough channel surfaces [64]. We investigated the influence of different types of roughness on the position of the effective boundary h_{eff} . Further, we have shown how the effective boundary depends on the distribution of the roughness elements and how roughness and hydrophobicity interact with each other [65]. We were also able to simulate flow over surfaces generated from AFM data of gold coated glass used in microflow experiments by Vinogradova and Yakubov [66]. We found that the height distribution of such a surface is approximately Gaussian and that a randomly arranged surface with a similar distribution gives the same result for the position of the effective boundary although in this case the heights are not correlated [64]. Currently, we model AFM based measurements to determine lubrication forces in order to probe the fundamental

concept of boundary conditions leading to a slippage or a shift of the effective boundary position [67, 68].

A natural continuation of our previous works on roughness induced apparent boundary slip is the analysis of flow along superhydrophobic surfaces as presented in this article. It has been recently predicted [69] and experimentally reported [70] that the so-called Fakir effect or Cassie state considerably amplifies boundary slippage on superhydrophobic surfaces. Using highly rough hydrophobic surfaces such a situation can be achieved. Instead of entering the area between the rough surface elements, the liquid remains at the top of the roughness and traps air in the interstices. Thus, a very small liquid-solid contact area is generated. In this article we quantify the slip in such systems using Couette and Poiseuille flow, where the flow is confined between two parallel walls separated by a distance $2d$. In our simulations, the lower wall is static and is patterned with holes or grooves to which vapor bubbles are trapped. The upper one is smooth and can be driven with shear velocity u_0 in the case of a Couette setup. The system boundaries are periodic and a unit cell of the regular array is included in a simulation. To trap bubbles to holes, some heterogeneity is needed at the edges of holes in order to pin the contact line. To this end, we use different wettabilities for boundaries in contact with the main channel and with the hole. For a Couette setup, the effective slip length can be calculated from the shear stress $\sigma = \mu du/dz$ acting on the upper wall, which is obtained from the no-slip boundary condition imposed at the fluid-solid boundaries. Thus, the effective slip length reads as $b = \mu u_0/\sigma - 2d$, where μ is the dynamic viscosity of the liquid. In case of a Poiseuille flow, a driving body force is applied effectively generating a pressure gradient $\frac{\partial P}{\partial z}$. Assuming Navier's boundary condition, b is measured by fitting the theoretical velocity profile as given by

$$u_z(x) = \frac{d^2}{2\mu} \frac{\partial P}{\partial z} \left[\frac{-x^2}{2d^2} + \frac{x}{d+b} + \frac{2b}{d+b} \right] \quad (10)$$

to the simulated data via the slip length b . This flow profile assumes the lower boundary to have a slip while on the upper wall a no-slip boundary condition is applied.

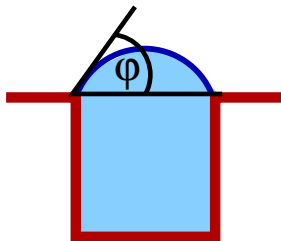


Figure 1. Definition of the protrusion angle φ .

The parameter G_b is chosen such that the density ratio between liquid and gas is between 22 and 44. This ratio is too small for a realistic description of gas bubbles in a liquid. Also, the interface between both phases is of finite width causing the resistance in the vapor phase. However, these limitations of multiphase LB models do not influence the qualitative insight obtained from the simulations.

In equivalence to the definition of the contact angle, which is not suitable for bubble mattresses as studied in this paper, we utilize the so-called protrusion angle φ to classify the bubbles in the simulated systems. The protrusion angle is defined by measuring the angle between the surface and a tangent at the bubble surface (see Fig. 1). The protrusion angle can be varied in the simulations by changing the bulk pressure of the liquid phase.

3. Results

3.1. Surfaces patterned with microgrooves

A surface structure that has been studied both experimentally and theoretically in great detail consists of longitudinal grooves etched in a smooth surface. If such grooves are hydrophobic, they can be filled with vapor forming cylindrical bubbles that are surrounded by liquid. The surface between individual grooves is hydrophilic causing an effective pinning of the three-phase contact line. In simulations, such hydrophilic surfaces can be obtained by setting a virtual surface density of the same order as the liquid density when computing the fluid-surface interactions as given by Eq. 9. The hydrophobic interactions are generated in a similar fashion by choosing a substantially smaller value for the virtual surface density. Fig. 2 shows a 3D visualization of the simulated unit cell. The length of the system is $L = 40$ lattice units and the width of the groove is defined by c resulting in a distance between two grooves given by $(L - c)$ lattice units. The height of the channel is $d = 135$ lattice units in x -direction, where the top of the system is defined by a smooth no-slip surface. The flow is generated by a constant body force acting in z -direction effectively resulting in a Poiseuille profile. Apart from the top and bottom plane, all boundaries are periodic.

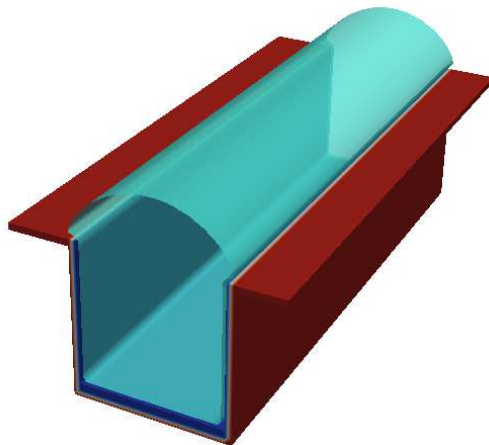


Figure 2. 3D visualization of a grooved surface. The width of the unit cell is L and the width of a groove is defined by c .

A similar system was investigated in the experiments by Tsai et al. [29]. They

studied the flow field over gas filled grooves oriented in flow direction by using micro particle image velocimetry (micro PIV). In [29] they presented measured flow profiles and the corresponding effective slip lengths. The behavior of the slip length in dependence on different geometrical parameters has been investigated and it was concluded that the obtained values for slip length cannot be explained by the theory of Philip [71] which provides an analytical model for slip flow on striped full-slip / no-slip surfaces. Their explanation was that due to the meniscus forming the bubble surface the no-shear (i.e. full-slip) parts develop an additional drag, similar to the effect reported by Richardson who showed that a rough no-shear surface creates sufficient drag to obtain macroscopically a no-slip boundary [59].

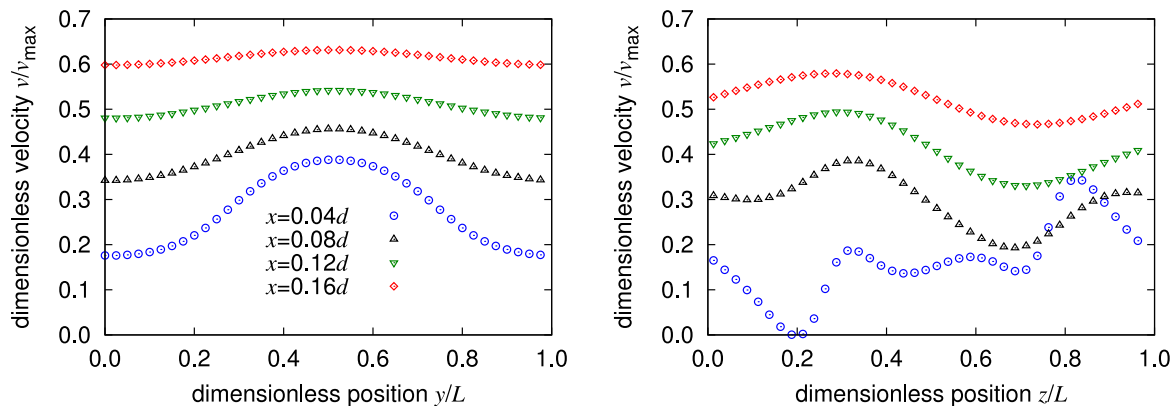


Figure 3. Flow profile perpendicular to the grooves for flow parallel (left) and perpendicular (right) to the grooves at different x positions over the surface. The groove is located in the centre of the system between $0.25L$ and $0.75L$. In the left panel a strong increase of the velocity in close vicinity to the bubble can be seen that relaxes within $0.16d$ to an almost undisturbed flow. The right plot demonstrates that flow perpendicular to the grooves causes more significant disturbances, which get still damped rather quickly.

Following the work of Tsai et al. we first present simulations of flow over grooves oriented in flow direction. The width of the groove is chosen to be $c/L = 0.5$. The protrusion angle in the experiments and in the simulations is chosen to be $\varphi = -10^\circ$, i.e., the liquid-gas interface forms a dimple rather than a bubble. The meniscus increases the vapor covered area (no-shear surface) but also introduces roughness that leads to a higher friction and therefore a reduced slip. In Fig. 3 we show the flow profile over one groove for different distances from the surface. At a very close distance $x = 0.04d$ the bubble has a strong influence on the flow, since the velocity in the centre of the groove is more than twice as large as the velocity in the centre of the void space. This effect is damped very quickly, i.e., at $x = 0.16d$ the velocity increase in the area above the bubble is less than 10% compared to the undisturbed case. The strong damping allows the treatment of such a grooved surface as a surface with an effective boundary position. The flow profiles are consistent with the results of Tsai et al. who also found a strong increase of the velocity above the grooves that is damped strongly further in the bulk. Further, the measured and the simulated slip lengths b/L are of the order of

half the theoretical prediction by Philip [71]. The reason for this is the assumption of a flat surface with stripes of no-slip and no-shear, while in the case of vapor filled grooves a meniscus is formed introducing an additional roughness that reduces the slip of the fluid over the surface.

In order to compare our results to the theoretical results of Lauga and Davis [26], we also consider grooves which are oriented perpendicular to the flow. In the right panel of Fig. 3, we show the flow profile in the vicinity of a perpendicular groove as it is assumed by the theory. Interestingly, here the flow velocity does not increase as strongly as in the aligned case above the groove but right after it. Again, a deceleration in front of the groove can be observed and the flow profiles are not symmetric towards the centre of a unit cell which is caused by the driving direction of the flow. The disturbances caused by the bubble are not damped as quickly as in the case of longitudinal grooves. For example, even at $x = 0.16d$ the flow velocity changes between $0.45v_{\max}$ and $0.59v_{\max}$. Further the disturbance close to the boundary is much stronger. At $x = 0.04d$ one can see a strong decrease of the velocity at the beginning of the groove and a strong increase at the end. The reason is the dimple shape of the meniscus. This leads to a compression of the streamlines at the end of the meniscus which is equivalent to an increased velocity. The dependence of the slip length on the orientation is consistent with the work of Bazant et al. who have shown for flat stripes that a generalized tensor form would be required to describe the surface properly [72].

The shape of the meniscus has a significant influence on the slip length. The above mentioned analytical approach of Davis and Lauga described the effective slip length in dependence on the protrusion angle φ on a surface with grooves perpendicular to the flow direction [26]. The theory assumes rigid bubbles with a full-slip surface, which corresponds an infinitely thin liquid-gas interface and vanishing gas density. In this case the slip length is given by

$$\frac{b}{c} = \pi \left(\frac{c}{L} \right) \int_0^\infty A(s) ds, \quad (11)$$

with

$$A(s) = \frac{s}{\sinh 2s(\pi - \varphi) + s \sin 2\varphi} \times \left[\cos 2\varphi + \frac{s \sin 2\varphi \cosh s\pi + \sinh s(\pi - 2\varphi)}{\sinh s\pi} \right]. \quad (12)$$

The only parameters entering the calculation of the effective slip length b are the protrusion angle φ and the ratio between the width of a groove c and the length of a unit cell L . The actual values of the slip length have to be calculated numerically.

In Fig. 4 we show the dimensionless slip length b/L versus the protrusion angle φ as given by Eq. 11 and by the simulation. The system length in this case is $L = 40$ lattice units and the width of a groove is $c = 30$ lattice units. The protrusion angle is measured by fitting a circle to the cross section of the interface. Since the interface between the vapor and the liquid is diffuse, the actual bubble position is not strictly defined. This is in contrast to the theoretical solution and renders the determination of the protrusion angle difficult. Therefore, we apply different threshold values ϱ_t for the fluid density at the interface to determine the protrusion angle. This value has to

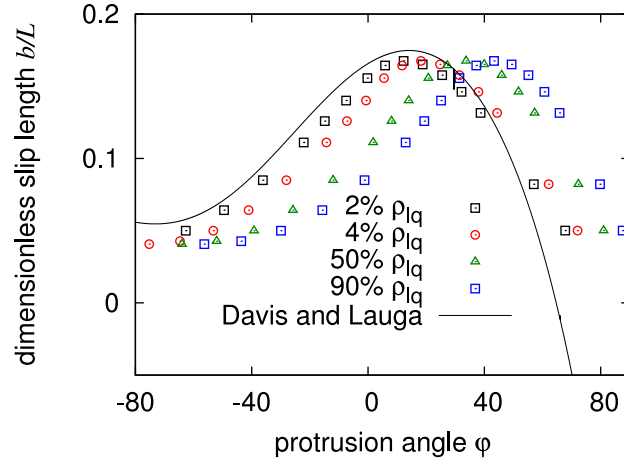


Figure 4. Slip length versus protrusion angle φ for different threshold values. The groove has a width of $c = 30$ and the system length is $L = 40$. Since the multiphase lattice Boltzmann model used is a diffuse interface model, the protrusion angle is not defined uniquely but depends on where the actual interface position is assumed, i.e. which threshold ϱ_t is chosen. Due to the non perfect slip on the vapor phase the analytical solution by Lauga et al. is scaled down by a factor of 0.75.

be somewhere between the high (liquid) density $\varrho_{lq} = 2.2$ and the lower (gas) density $\varrho_g = 0.05$. In Fig. 4 the effect of choosing different threshold values between $\varrho_t = 0.02\varrho_{lq}$ and $0.9\varrho_{lq}$ is demonstrated. Here, it can be observed that a variation of the threshold can lead to a shift in the protrusion angle of more than 20° .

By comparing the simulation data to the results of Davis and Lauga Eq. 11, we find that the qualitative shape of the curve is well reproduced, i.e., the slip length first increases with rising φ up to a maximum at φ_{\max} and then follows a steep decrease for high φ . As will be shown later, it eventually can even become negative. However, in addition to the possible variation of φ we find a second deviation between theory and simulation: the detected slip length b is lower than predicted by Davis and Lauga. To be able to compare theory and simulation, the theoretical values are scaled by a factor of 0.75 to fit the data. This can be explained by the fact that the diffuse interface must not be described by a smooth full slip cap. Instead it shows a finite slip due to the friction within the interface region. Further, the density ratio between liquid and vapor is limited in the lattice Boltzmann model used. In the presented case it is only $1/44$. Therefore, the shear resistance on the bubble surface is only reduced by this factor, while in a real system consisting of, e.g., water and air, this ratio would be of the order of $1/1000$ rendering the assumption of no shear more realistic. Apart from the shift due to the finite interface width, the simulation is able to recover the main conclusions from the theory.

We further investigate the influence of the area covered by the bubble $\phi = c/L$ on the slip length. Different channel widths are been investigated for different protrusion angles φ . The threshold value determining the interface position was chosen to be $\varrho_t = 0.04\varrho_{lq}$. Our results are shown in Fig. 5. The qualitative behavior of the results

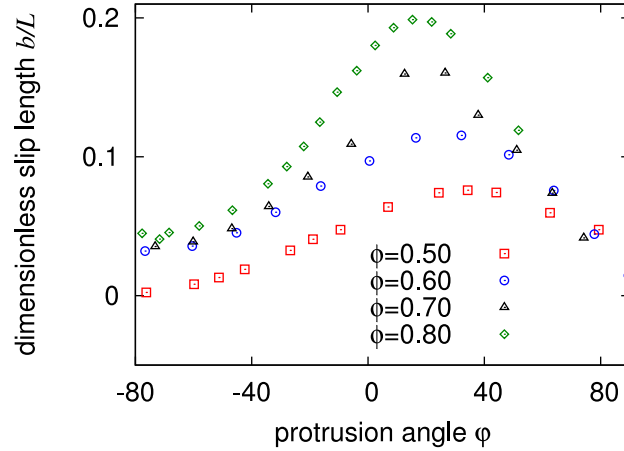


Figure 5. Normalized slip length b/L versus the protrusion angle φ , for different ratios between the width of the grooves c and the system length L . The behavior is similar to the prediction of Eq. 11. Further, a larger $\phi = c/L$ leads to a strong increase of the slip length.

again follows Eq. 11. The maximum slip length is increased very strongly by increasing the relative width of the groove. An increase of the surface coverage from $\phi = 0.5$ to 0.8 leads to an increase of the dimensionless slip length where the values for the respective maxima range from $b/L = 0.07$ to 0.19 . Such a strong increase is also predicted by Eq. 11. Further, due to the influence of the increased roughness for $\varphi > 60^\circ$ the slip length becomes smaller for larger φ . Also for $\varphi < -40^\circ$ the slip becomes smaller than $b < 0.05L$ and nearly independent on the surface coverage ϕ .

To conclude, in the current section we have introduced our simulation methodology and demonstrated that it is well suited to reproduce experimental flow profiles and to study the influence of the protrusion angle φ on a detected effective slip. However, it has to be taken into account that the simulation model is a diffuse interface method effectively rendering our bubbles to be on the nanoscale. A comparison with the theoretical description of Davis and Lauga demonstrates that the diffuse interface can have a strong effect on the actual slip which has to be considered when designing surfaces with nanoscale patterns for specific applications.

3.2. Spherical nanobubbles

Steinberger et al. utilized surfaces patterned with a square array of cylindrical holes to demonstrate that gas bubbles present in the holes may cause a reduced slip [24]. Numerically, they found even negative slip lengths for flow over such bubble mattresses, i.e., the effective no-slip plane is inside the channel and the bubbles increase the flow resistance. Motivated by Steinberger's work, we consider negative slip lengths on bubble covered surfaces and also discuss the question of shear-rate dependent slip. In particular, we demonstrate that bubbles can generate a shear-rate dependence of the detected slip length. The current section is a review of the studies presented in [25, 58] and here we relate them to recent references in the literature and newer findings as presented in

remainder of this contribution.

The distance between top and bottom walls is $d = 40$ lattice nodes in all simulations in this section and the area fraction of holes is kept at 0.43. Similar to the previous section, a unit cell of the regular array is included in a simulation and periodic boundary conditions are applied at domain boundaries.

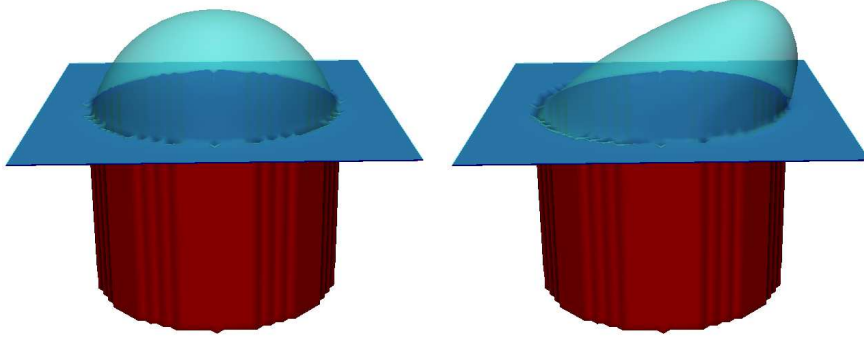


Figure 6. 3D visualization of a spherical bubble. While the left panel shows the undisturbed shape, the right panel demonstrates the deformation of the bubble under strong shear.

We investigate the effect of a modified protrusion angle and different surface patterns by using square, rectangular, and rhombic bubble arrays. The cylindrical holes have a radius $a = 20$ lattice units and the area fraction of the holes is equal in all cases. The shear rate is such that the Capillary number $Ca = \mu a G_s / \gamma = 0.16$. Here, G_s and γ are the shear rate and surface tension, respectively. A snapshot of a simulated system is shown in the left part of Fig. 6. The slip lengths obtained for differently shaped unit cells and protrusion angles are shown in Fig. 7. Following the discussion on the diffuse interface and the definition of the protrusion angle as given in the previous section, we choose the threshold value for the density defining the interface to be at $\rho_t = 0.5\rho_{lq}$. The observed behavior is similar to that reported in [24], where a square array of holes was studied. In particular, we observe that when φ is large enough b becomes negative. Moreover, for the case presented in the current paper the slip length is maximized when the protrusion angle is close to zero. In practical applications, this would allow the highest possible throughput in a microchannel to be obtained. The behavior of the slip length can be explained by thinking of an increased surface roughness if the protrusion angle is larger or smaller than zero which is in competition with the increased area of low friction in the case of large bubbles. Since the area fraction of the bubbles is kept constant for all three different unit cells, our results clearly indicate that slip properties of the surface can be tailored not only by changing the protrusion angle but also by the array geometry. In the presented study, the highest slip lengths are obtained for the rhombic unit cell.

Generally, our findings are in accordance to the results presented in the previous section as it has been confirmed in the theoretical paper of Davis and Lauga [26]. Obviously, also here the limitations of the comparison due to the diffuse interface

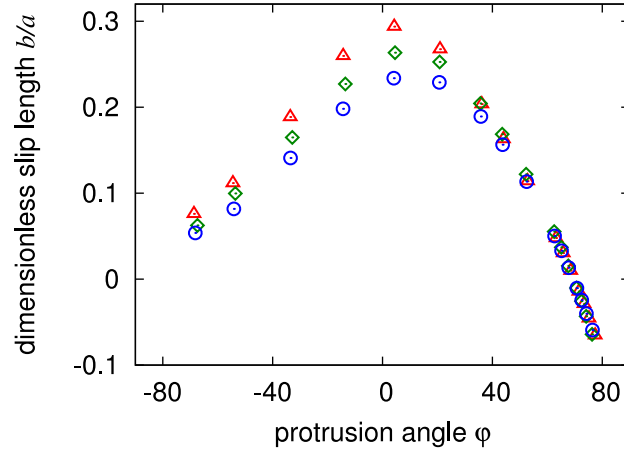


Figure 7. Slip length b as a function of the protrusion angle ϕ . Corresponding results are given for a rhombic array (triangles), a rectangular array (diamonds), and a square array (circles).

and finite density ratio of the liquid and gas phases still hold. In addition, the simulated system is now three dimensional while Davis and Lauga only considered a two-dimensional case.

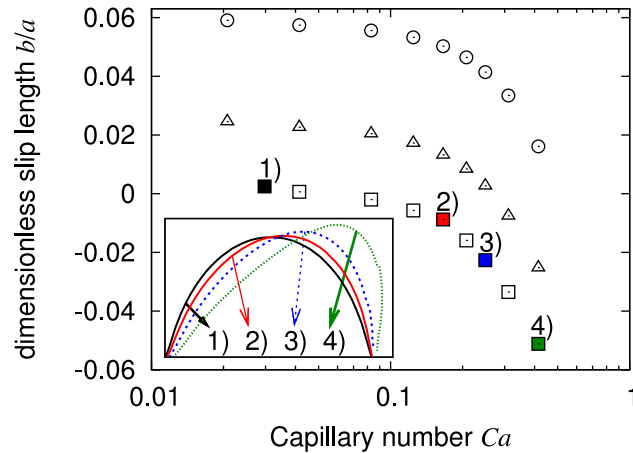


Figure 8. The slip length b as a function of the capillary number Ca for a square array of spherical bubbles with three different protrusion angles, $\varphi = 63^\circ, 68^\circ,$ and 71° (from uppermost to lowermost) is shown. The inset depicts cross sections of liquid-gas interfaces for four capillary numbers and $\varphi = 71^\circ$ [25].

In the following, the shear-rate dependence of the slip length is investigated. As the shear rate and thus the viscous stresses increase the bubbles are deformed and the flow field is modified. An example of such a deformed bubble is shown in Fig. 6 (right). In Fig. 8, we show the simulated normalized slip length b/a as a function of the Capillary number for three different protrusion angles. The Capillary numbers chosen are at the higher end of the experimentally available range. The inset of Fig. 8 shows cross sections of the liquid gas interface of a bubble with protrusion angle $\varphi = 71^\circ$ demonstrating the correlation between shear rate and deformation. Our lattice Boltzmann simulations

clearly show shear-rate dependent slip, but the behavior is opposite to that found in some experiments: in fact, the slip lengths measured by us decrease with increasing shear due to a deformation of the bubbles which effectively reduces the roughness of the surface. In the experiments, surface force apparatuses are used (see, e.g., Ref. [19]), where a strong increase in the slip is observed after some critical shear rate. This shear-rate dependence has been explained, e.g., with formation and growth of bubbles [11, 73]. In our simulations, there is no formation or growth of the bubbles as we only simulate a steady case for given bubbles. The experiments on the other hand are dynamic. However, our results indicate that the changes in the flow field which occur due to the deformation of the bubbles cannot be an explanation for the shear-rate dependence observed in some experiments. Our results are consistent with [64], where it is shown that smaller roughness leads to smaller values of a detected slip. In the present case, the shear reduces the average height of the bubbles and thus the average scale of the roughness decreases as well. However, a possible explanation of the dependence of the slip length on the shear rate was recently given by Gao and Feng [27]. They argue that the experimentally observed increase of b can be explained by a depinning of the three-phase contact line resulting in the extreme case in a continuous gas film on the surface. Such a behavior is omitted in our simulations since the interface between liquid and gas favours to stay at the edge of a hole due to the different wettabilities inside the holes and on the top of the surface which effectively results in a contact-line pinning.

3.3. Bubble-size distributions

As already stated in the introduction, in all previous contributions to the literature concerning slip flow over a bubble mattress, only mattresses which consist of evenly sized bubbles are taken into account. However, such a situation is not necessarily realistic since in reality some kind of imperfections are inevitably present. Therefore, this section focuses on mattresses with bubbles of different size. For the sake of simplicity we restrict ourselves to two different sizes only. In practice, such a situation can be achieved by structuring the surface with holes that have different radii. The height of the bubbles occurring on such a structuring can be tuned by variation of the bulk pressure. For a given bulk pressure, bubbles located in larger holes protrude stronger to the flow channel than those in the smaller ones. We show that the bubble-size distribution can significantly affect the slip behavior and, e.g., decrease the negative slip caused by strongly protruding bubbles. While this reduction may hamper experimental observations of negative slip, it is an attractive candidate for designing bubble surfaces aiming to maximal flow slippage.

The geometrical setup used in the present simulations is shown in Fig. 9. As in the previous section we simulate a Couette flow between two parallel plates, where one of the plates is smooth and another is patterned with an array of cylindrical holes. The holes form two nested square arrays such that one of the arrays consists of holes with radius a_1 and the other one of holes with radius a_2 . A set of four unit cells of the

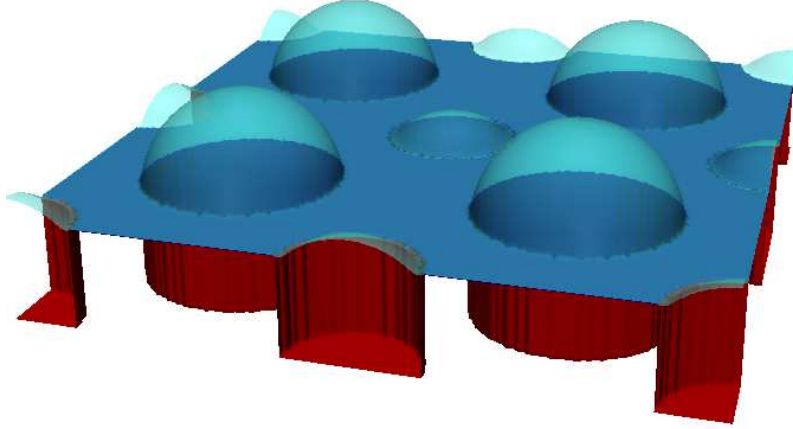


Figure 9. Visualization of the simulation setup. Four unit cells are shown. Each has small bubbles (radius a_2) at four edges of the cell connected through periodic boundary conditions, and a large bubble at the centre of the cell (radius a_1). Thus, the bubble mattress consists of two nested square arrays of bubbles. In the case shown $a_2/a_1 = 0.67$. The upper wall is smooth and it is moved with constant speed to achieve a shear flow.

system is shown in Fig. 9. In all simulations, a_1 is fixed to 30 lattice units and a_2 varies between 20 and 30 lattice units. The system size is adjusted accordingly such that the area fraction of the holes is $\phi = 0.42$ regardless of the value of a_2 . Notice that when the radii a_1 and a_2 are unequal, the protrusion angles related to the respective holes are also unequal for a given value of the bulk pressure.

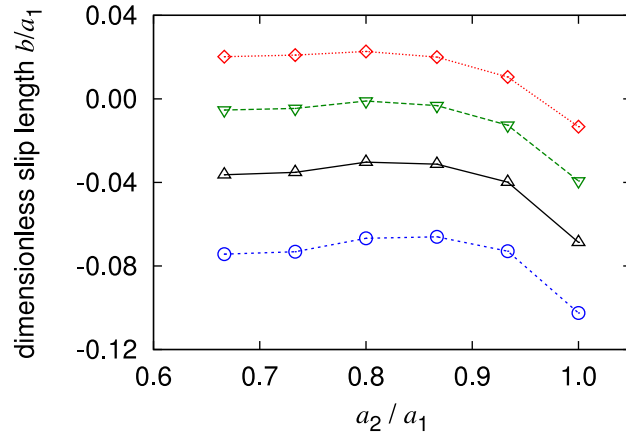


Figure 10. Slip length as a function of the ratio a_2/a_1 . The curves are for different values of bulk pressure such that the protrusion angle of the larger bubbles are $\varphi = 80^\circ, 76^\circ, 73^\circ$, and 70° from bottom to top. The shear rate is fixed and corresponds to capillary number $Ca = 0.11$.

First we investigate how a variation of the size of the smaller holes affects the effective slip. As the radius a_2 is reduced, also the protrusion angle of the bubbles attached to the smaller holes decreases, i.e., these bubbles become flatter. In previous investigations [24–26] it has been shown for the case of mono-sized protruding bubbles,

that when the protrusion angle decreases, the slip length is increased due to the reduced roughness of the bubble mattress. On the basis of these findings, one could expect that when the radius a_2 is reduced, the slip length decreases despite the fact that the radius of the larger holes is kept constant. The simulation results, as shown in Figs. 10 and 11, show that this is indeed the case for small changes in the size of smaller holes. However, when the size difference between larger and smaller holes is increased such that $a_2/a_1 \approx 0.8$, a maximum in the effective slip length is observed and thereafter, for even smaller values of a_2/a_1 , the slip length starts to decrease. This observation can be understood as a competition of two different factors affecting the slip phenomenon. The first one is related to the above described flattening of the smaller bubbles, which dominates at ratio a_2/a_1 close to unity. However, as the size of the smaller holes is further reduced, the area fraction of the smaller bubbles also decreases as well as their effect on the total effective slip. On the same basis, one might expect that as $a_2/a_1 \rightarrow 0$, slip approaches the same value as for $a_2/a_1 = 1$. However, as the former case corresponds to a square array of bubbles and the latter to a rhombic one, the actual values of slip length may be different as shown in Ref. [25] or Sec. 3.2.

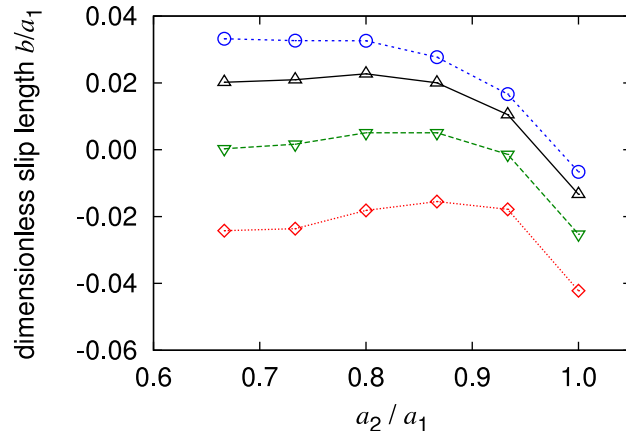


Figure 11. Slip length as a function of the ratio a_2/a_1 . The curves are for different shear rates corresponding to $Ca = 0.036, 0.11, 0.18$, and 0.25 from top to bottom. The bulk pressure is fixed such that the protrusion angle of the large bubbles is $\varphi = 70^\circ$.

In Fig. 10 we show how the bulk pressure affects the slip length. One can see that when the pressure is increased (i.e., the protrusion angle φ is decreased), also the effective slip length increases. This is due to the decreasing overall roughness as the height of all bubbles in the system is reduced. From Fig. 10 we also observe that the maximum of the slip length becomes less pronounced and shifts towards smaller values of ratio a_2/a_1 as the bulk pressure increases. This behavior is reasonable as in this case the difference in the heights of larger and smaller bubbles is reduced (see Fig. 12).

Finally we consider the effect of shear rate on the slip length. It was previously shown in section 3.2 that increasing shear rates cause the slip length to decrease. This dependence is related to the reduced height of the roughness as the shear deforms the

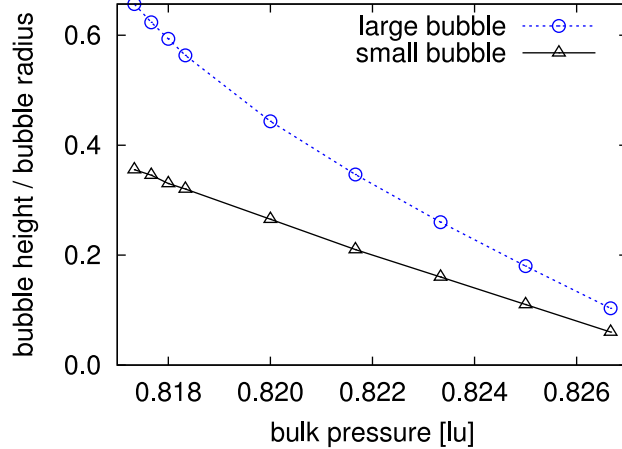


Figure 12. Bubble height in large and small holes with different bulk pressures (given in lattice units).

bubbles (see also Ref. [64]). Similar behavior is found also for the mattress with bimodal bubble-size distribution (see Fig. 11). However, we point out that it has recently been shown that depinning of the contact line at high shear rates may lead to formation of continuous gas film on the surface, and this depinning transition may change the qualitative behavior of the shear-rate dependence [27]. In the present work, contact lines are pinned on the hole edges at all shear rates.

To summarize, in this section we simulated laminar flow past bubble arrays consisting of bubbles of two different sizes, and studied the flow slippage caused by the bubbles. The slip behavior was found to differ from that previously found for surfaces made up of evenly sized bubbles. The observed difference is due to the additional larger-scale roughness that results from the more complex surface geometry. The presented results indicate that even rather small non-uniformity in the mattress may considerably increase the slip and thus complicate the observation of negative slip. On the other hand, as the negative slip is usually an unwanted property from the application point of view, non-uniformity and disorder could be utilized to prevent negative slip and increase the throughput in microfluidic devices.

4. Conclusion

To conclude, we presented lattice Boltzmann simulations of laminar flow past structured surfaces which are covered with nanobubble arrays. After a qualitative comparison to experimentally observed flow over cylindrical bubbles we demonstrated that our simulations are able to reproduce the general features predicted by the theoretical description of Davis and Lauga. However, for a quantitative comparison the theory needs to be extended to take into account diffuse liquid-gas interfaces as well as a finite density difference between liquid and gas. By studying arrays consisting of spherical bubbles we demonstrated that a strong shear can deform the bubbles and thus reduce

the apparent roughness of the surface. As a consequence the effective slip is reduced. We have further shown that patterned surfaces can be designed for maximal slippage by variation of the position of the bubbles as well as by utilizing a distribution of their size. Our results can be utilized to develop micropatterned superhydrophobic surfaces for specific microfluidic applications where a local variation or an especially high value of the effective slip might be used to direct flow or to maximize the throughput in a microchannel. Further, we believe that our results can contribute to the understanding of some controversially discussed experimental results on the shear rate dependence of boundary slippage.

Acknowledgments

This work was supported by the DFG priority program “nano- and microfluidics” (project Ha 4382/2-1), the Academy of Finland (project 135857) and under the HPC-EUROPA2 project (project 228398). The computations were performed at the Jülich Supercomputing Centre, the Scientific Supercomputing Centre Karlsruhe, and SARA Amsterdam.

References

- [1] P. Tabeling. *Introduction to microfluidics*. Oxford University Press, 2005.
- [2] E. Lauga, M. P. Brenner, and H. A. Stone. *Microfluidics: the no-slip boundary condition, in handbook of experimental fluid dynamics*, chapter 15. Springer, 2005.
- [3] V. S. J. Craig, C. Neto, and D. R. M. Williams. *Phys. Rev. Lett.*, 87:054504, 2001.
- [4] D. C. Tretheway and C. D. Meinhart. *Phys. Fluids*, 16:1509, 2004.
- [5] J. T. Cheng and N. Giordano. *Phys. Rev. E*, 65:031206, 2002.
- [6] C. H. Choi, K. J. Westin, and K. S. Breuer. *Phys. Fluids*, 15:2897, 2003.
- [7] J. Baudry and E. Charlaix. *Langmuir*, 17:5232, 2001.
- [8] C. Cottin-Bizonne, S. Jurine, J. Baudry, J. Crassous, F. Restagno, and E. Charlaix. *Eur. Phys. J. E*, 9:47, 2002.
- [9] O. I. Vinogradova and G. E. Yakubov. *Langmuir*, 19:1227, 2003.
- [10] O. I. Vinogradova. *Langmuir*, 11:2213, 1995.
- [11] P. Gennes. *Langmuir*, 18:3413, 2002.
- [12] S. Succi. *Phys. Rev. Lett.*, 89:064502, 2002.
- [13] J. L. Barrat and L. Bocquet. *Phys. Rev. Lett.*, 82:4671, 1999.
- [14] M. Cieplak, J. Koplik, and J. R. Banavar. *Phys. Rev. Lett.*, 86:803, 2001.
- [15] P. A. Thompson and S. Troian. *Nature*, 389:360, 1997.
- [16] D. Tretheway, L. Zhu, L. Petzold, and C. Meinhart. In *2002 ASME International Mechanical Engineering Congress & Exposition, New Orleans, Louisiana, 2002*.

- [17] C. Neto, D. R. Evans, E. Bonaccorso, H. J. Butt, and V. S. J. Craig. *Rep. Prog. Phys.*, 68:2859, 2005.
- [18] N. V. Churaev, V. D. Sobolev, and A. N. Somov. *J. Colloid Int. Sci.*, 97:574, 1984.
- [19] Y. Zhu and S. Granick. *Phys. Rev. Lett.*, 87:096105, 2001.
- [20] L. Bocquet and J. L. Barrat. *Soft Matter*, 3:685, 2007.
- [21] C. L. M. H. Navier. *Mem. Acad. Sci. Ins. Fr.*, 6:389, 1823.
- [22] C. Cottin-Bizonne, B. Cross, A. Steinberger, and E. Charlaix. *Phys. Rev. Lett.*, 94:056102, 2005.
- [23] O. I. Vinogradova, K. Koynov, A. Best, and F. Feuillebois. *Phys. Rev. Lett.*, 102:118302, 2009.
- [24] A. Steinberger, C. Cottin-Bizonne, P. Kleimann, and E. Charlaix. *Nature Materials*, 6:665, 2007.
- [25] J. Hyväluoma and J. Harting. *Phys. Rev. Lett.*, 100:246001, 2008.
- [26] A. M. J. Davis and E. Lauga. *Phys. Fluids*, 21:011701, 2009.
- [27] P. Gao and J. J. Feng. *Phys. Fluids*, 21:102102, 2009.
- [28] C. J. Teo and B. C. Khoo. *Microfluid. Nanofluid.*, 2010.
- [29] P. Tsai, A. M. Peters, C. Pirat, M. Wessling, R. G. H. Lammertink, and D. Lohse. *Phys. Fluids*, 21:112002, 2009.
- [30] C. Cottin-Bizonne, C. Barentin, E. Charlaix, L. Bocquet, and J. L. Barrat. *Eur. Phys. J. E*, 15:427, 2004.
- [31] N. V. Priezjev, A. Darhuber, and S. Troian. *Phys. Rev. E*, 71:041608, 2005.
- [32] G. H. Tang, W. Q. Tao, and Y. L. He. *Phys. Fluids*, 17:058101, 2005.
- [33] M. Sbragaglia and S. Succi. *Phys. Fluids*, 17:093602, 2005.
- [34] S. Ansumali and I. V. Karlin. *Phys. Rev. E*, 66:026311, 2002.
- [35] V. Sofonea and R. F. Sekerka. *Phys. Rev. E*, 71:066709, 2005.
- [36] X. D. Niu, C. Shu, and Y. T. Chew. *Europhys. Lett.*, 67:600, 2004.
- [37] Z. Guo, B. Shi, T. S. Zhao, and C. Zheng. *Phys. Rev. E*, 76:056704, 2007.
- [38] X. Nie, G. D. Doolen, and S. Chen. *J. Stat. Phys.*, 107:279, 2002.
- [39] L. Zhu, D. Tretheway, L. Petzold, and C. Meinhart. *J. Comp. Phys.*, 202:181, 2005.
- [40] R. Benzi, L. Biferale, M. Sbragaglia, S. Succi, and F. Toschi. *Europhys. Lett.*, 74:651, 2006.
- [41] J. Zhang and D. Y. Kwok. *Phys. Rev. E*, 70:056701, 2004.
- [42] R. Benzi, L. Biferale, M. Sbragaglia, S. Succi, and F. Toschi. *Phys. Rev. E*, 74:021509, 2006.
- [43] H. Huang, D. T. Thorne, M. G. Schaap, and M. C. Sukop. *Phys. Rev. E*, 76:066701, 2007.
- [44] S. Schmieschek and J. Harting. *Submitted for publication*, 2009. arXiv:0910.3915.

- [45] J. Harting, C. Kunert, and H. Herrmann. *Europhys. Lett.*, pp 328–334, 2006.
- [46] H. Kusumaatmaja, J. Leopoldes, A. Dupuis, and J. M. Yeomans. *Europhys. Lett.*, 73:740, 2006.
- [47] H. Kusumaatmaja and J. M. Yeomans. *Langmuir*, 23:6019, 2007.
- [48] C. Pirat, M. Sbragaglia, A. M. Peters, B. M. Borkent, R. G. H. Lammertink, M. Wesseling, and D. Lohse. *Europhys. Lett.*, 81:66002, 2008.
- [49] J. Hyväluoma, A. Koponen, P. Raiskinmäki, and J. Timonen. *Eur. Phys. J. E*, 23:289, 2007.
- [50] N. Moradi, F. Varnik, D. Raabe, and I. Steinbach. *Europhys. Lett.*, 89:26006, 2010.
- [51] S. Succi. *The lattice Boltzmann equation for fluid dynamics and beyond*. Oxford University Press, 2001.
- [52] P. L. Bhatnagar, E. P. Gross, and M. Krook. *Phys. Rev.*, 94:511, 1954.
- [53] X. Shan and H. Chen. *Phys. Rev. E*, 47:1815, 1993.
- [54] X. Shan and H. Chen. *Phys. Rev. E*, 49:2941, 1994.
- [55] M. Sbragaglia, R. Benzi, L. Biferale, S. Succi, and F. Toschi. *Phys. Rev. Lett.*, 97:204503, 2006.
- [56] J. Horbach and S. Succi. *Phys. Rev. Lett.*, 96:224503, 2006.
- [57] S. Chibbaro, L. Biferale, F. Diotallevi, S. Succi, K. Binder, D. Dimitrov, A. Milchev, S. Girardo, and D. Pisignano. *Europhys. Lett.*, 84:44003, 2008.
- [58] J. Harting, C. Kunert, and J. Hyväluoma. *Microfluidics and Nanofluidics*, 8:1, 2010.
- [59] S. Richardson. *J. Fluid Mech.*, 59:707, 1973.
- [60] G. McHale and M. I. Newton. *J. Appl. Phys.*, 95:373, 2004.
- [61] A. Al-Zoubi and G. Brenner. *Computers & Mathematics with Applications*, 55:1365, 2008.
- [62] F. Varnik and D. Raabe. *Modelling Simul. Mater Sci Eng.*, 14:857, 2006.
- [63] F. Varnik, D. Dorner, and D. Raabe. *J. Fluid Mech.*, 573:191, 2006.
- [64] C. Kunert and J. Harting. *Phys. Rev. Lett.*, 99:176001, 2007.
- [65] C. Kunert and J. Harting. *Int. J. Comp. Fluid Dyn.*, 22:475, 2008.
- [66] O. I. Vinogradova and G. E. Yakubov. *Phys. Rev. E*, 73:045302(R), 2006.
- [67] C. Kunert, J. Harting, and O. I. Vinogradova. *Submitted for publication*, 2009.
- [68] C. Kunert and J. Harting. *Proceedings of the 2nd Micro and Nano Flows Conference*, ISBN 978-1-902316-72-7, 2009.
- [69] C. Cottin-Bizonne, J. L. Barrat, L. Bocquet, and E. Charlaix. *Nature Materials*, 2:237, 2003.
- [70] O. J. Perot and J. P. Rothstein. *Phys. Fluids*, 16:4635, 2004.
- [71] J. R. Philip. *J. Appl. Math. Phys.*, 23:353, 1972.

- [72] M. Z. Bazant and O. I. Vinogradova. *J. Fluid Mech.*, 613:125–134, 2008.
- [73] E. Lauga and M. P. Brenner. *Phys. Rev. E*, 70:026311, 2004.